HHS Public Access

Author manuscript

Opt Lett. Author manuscript; available in PMC 2015 May 06.

Published in final edited form as:

Opt Lett. 2015 May 1; 40(9): 2025–2028.

Single input state, single–mode fiber–based polarization sensitive optical frequency domain imaging by eigenpolarization referencing

Norman Lippok[1,2,*], **Martin Villiger**[1,2], **Chang–Su Jun**[1,2], and **Brett E. Bouma**[1,2,3]

[1]Harvard Medical School, Boston, MA 02115, USA

[2]Wellman Center for Photomedicine, Massachusetts General Hospital, Boston, MA 02114, USA

[3]Harvard–Massachusetts Institute of Technology, Program in Health Sciences and Technology, Cambridge, MA 02142, USA

Abstract

Fiber–based polarization sensitive OFDI is more challenging than free–space implementations. Using multiple input states, fiber–based systems provide sample birefringence information with the benefit of a flexible sample arm but come at the cost of increased system and acquisition complexity, and either reduce acquisition speed or require increased acquisition bandwidth. Here we show that with the calibration of a single polarization state, fiber–based configurations can approach the conceptual simplicity of traditional free–space configurations. We remotely control the polarization state of the light incident at the sample using the eigenpolarization states of a wave plate as a reference, and determine the Jones matrix of the output fiber. We demonstrate this method for polarization sensitive imaging of biological samples.

Polarization sensitive (PS) optical coherence tomography (OCT) and optical frequency domain imaging (OFDI) [1, 2] provides a functional contrast in scenarios where morphology alone is insufficient [3–6]. Using bulk optics, the incident polarization state at the sample is known and thus readily permits extraction of sample birefringence information due to a measurable polarimetric change [1,7]. Single–mode fiber–based PS systems offer a versatile sample arm but exhibit additional fiber birefringence, which causes a random change of the polarization state at the sample. Polarization maintaining (PM) fiber can avoid polarization state transformations [8, 9], but cross coupling between the polarization eigenmodes of the fiber can introduce artifacts. Methods that allow the use of standard single–mode fiber probe the sample with at least two input polarization states, either by discrete and successive modulation [10, 11], continuous modulation [12] or multiplexing [13, 14]. Although these methods circumvent the need for a specific polarization state at the sample, they increase system and acquisition complexity, and either reduce acquisition speed or require increased acquisition bandwidth. Reduced complexity is valuable from a commercial standpoint. Indeed, applications that only require a quasi– stationary sample arm with only marginal

[*]*Corresponding author: nlippok@mgh.harvard.edu*.

changes in the fiber optical path after sample selection (e.g. ophthalmology) give room for simplified implementations of single–mode fiber–based PS–OCT that do not require active components, several input polarization states, or PM fiber. A single input polarization state would facilitate faster post–processing by adapting the rather effortless analytic solutions of traditional bulk PS–OCT systems. To achieve this, Trasischker *et al.* demonstrated a single–mode fiber system through careful calibration of four fiber output polarization states by temporally placing an additional polarizer and detector into the corresponding optical paths [15]. Work by other groups demonstrated similar calibration efforts [16]. Unfortunately, cumbersome and time demanding calibrations are not feasible in practice and defeat the purpose of fiber–based systems. The need of additional temporal elements as well as any interruption of the optical path for calibration purpose is undesirable in the presence of patients.

Here we propose a simplified method of using a single–mode fiber–based system with a single input polarization state that requires the calibration of only one fiber transformation. We use the reflections of a wave plate as a reference to conveniently obtain a calibration within a few seconds and with a sample or patient in place. We determine the output fiber Jones matrix to correct for the polarization transformation on the detection path during reconstruction. In the following section we describe how one can realize this calibration by adjusting (referencing) a fiber output polarization state to an eigenpolarization of a linearly birefringent medium.

To describe eigenpolarization referencing, first consider a general system comprising a quarter–half–quarter wave plate combination. It can be easily shown that the eigenvectors, known as eigenpolarizations or principle states of polarization (PSP), of such a system span the entire Poincaré sphere (Fig. 1a). For comparison, Fig. 1b shows this for a system consisting of a quarter and half wave plate using a range of optical axes orientations. Red and black represent the 180° apart PSP pairs, respectively (in Stokes space). Indeed, an incident state of polarization (ISP) that is aligned with a PSP remains unchanged (i.e., eigenvector). In the present work, we used a PSP to reference the output polarization state of a single–mode fiber to circumvent the fiber polarization transformation towards the sample. To simplify our configuration, we applied PSP–referencing using only a quarter wave plate (QWP). Possible eigenvectors are presented in Fig. 1c. The principle concept of our experiments is illustrated in Fig. 1d. The fast axis of QWP1 was adjusted to the horizontal. We used a fiber polarization controller to select the polarization state at the sample arm fiber tip so that the Stokes vectors of the backscattered light at the QWP1 front (interface 1, blue) and back interface (interface 2, red) were the same. Knowing that the polarization state exiting the sample arm fiber was then linear and horizontal (aligned with the fast optical axis) or linear and vertical (aligned with the slow optical axis), we used a second QWP with a fast optical axis adjusted at 45° with respect to the first wave plate’s optical axis to obtain circularly polarized light incident at the sample. After successful calibration, the detected Stokes vector of the back interface of QWP1 (interface 2, red) and the Stokes vector of the sample surface (interface 3, green) span an angle of 180° in the Poincaré sphere (after double passing QWP2).

The detected Jones vector of QWP1's first interface (blue) can be written as $E_1' = J_f E°$, where J_f is the Jones matrix of the fiber path from the sample arm fiber tip to the interferometer output. In the case of an incident polarization state that is aligned with the wave plate's fast optical axis, $E_1 = [10]^T$, the detected Jones vector of QWP1's second surface (red) is $E_2' = E_2' = E_2' = E_1'$ and the detected Jones vector at the sample surface (green) is $E_3' = J_f J_{WP1}^T J_{WP2}^T J_{WP2} J_{WP2} E_1 = J_f [0 \quad 1]^T$, where $J_{WP1,2}$ is the Jones matrix of QWP1,2 with a fast optical axis at 0° and 45°, respectively. Furthermore, the Jones vector after double passing the sample to some depth, z, is $E_z' = J_f J_{WP1}^T J_{WP2}^T J_s J_{WP2} J_{WP1} E_1$, where J_s is the round trip Jones matrix of the sample. Using E_2' and E_3', we can write the polarization evolution from the sample arm fiber tip to the interferometer output in matrix formalism,

$$\begin{pmatrix} E_{2x}' & E_{3x}' \\ E_{2y}' & E_{3y}' \end{pmatrix} = J_f \begin{pmatrix} 1 & 0 \\ 0 & 1 \end{pmatrix} \quad (1)$$

In our case, the input matrix merely equals the identity matrix and the output fiber Jones matrix is conveniently given by the measured Jones vectors $E^{2\prime}$ and $E^{3\prime}$. Note that if an ISP is aligned with the slow axis of QWP1, the identity matrix simply becomes anti–diagonal. Using the fiber Jones matrix, we can retrieve the sample Jones vector before QWP2, $\tilde{E}_z = \left(J_{WP1}^T\right)^{-1} J_f^{-1} E_z'$ and which corresponds to the signal acquired in traditional bulk PS–OCT. Accumulated retardation, δ_z , and optical axis orientation, θ_z , can then be extracted as reported previously, $\delta_z = \quad arctan\left(\tilde{E}_{zy}/\tilde{E}_{zx}\right)$, $\theta_z = (\pi - \Delta\varphi_x)/2$ is the phase difference between the orthogonal vector components of $\tilde{E}_z$ [1, 7]. Alternatively, the returning Jones vector after double passing the sample can be obtained, $E_z = \left(J_{WP2}^T\right)^{-1} \tilde{E}_z$. Accumulated sample retardation and optical axis orientation can be calculated in Stokes space as described in Ref. [17]. After spatial averaging in Stokes space using a Hanning– shaped kernel, extending over $w_z = 3r_z$ and $w_x = 3r_x$, with $r_{z,x}$ the the axial and lateral resolution, i.e. speckle size, respectively, we obtain the local retardation $\partial\delta_z/\partial z$, as well as the degree of polarization uniformity, DOPU = $[\Sigma_{\{n\}} \langle s_n\rangle^2]^{½} / \langle s_0\rangle$ where $\langle s_n\rangle$ is a spatially averaged Stokes parameter.

To obtain a better appreciation for the required alignment accuracy of the two wave plates in the sample arm, we simulated the error (offset) in the calculated retardation for several sample set retardations and fast axis orientations of QWP1 (Fig. 2a), as well as different retardation of the second wave plate (Fig. 2b). We assumed an ISP at QWP1 of $[10]^T$ as derived for Eq. 1 and a solution for the retardation known from Ref. [1,7]. Recall that in our derivation we assumed an axis of 0° for QWP1 and a retardation of 90° for the second wave plate. We note that the optical axis of QWP1 has a margin of ±3° from the horizontal and the retardation of QWP2 a margin of ±4° from the expected 90°, to yield a retardation error not larger than ±4° (shown by yellow lines).

Figure 3 depicts the single-mode fiber PS–OFDI system used for experimental validation. A custom wavelength swept laser offered 50 kHz sweep repetition rate with a 100 % duty

cycle (DC) and 80 mW average output power. The center wavelength was 1298 nm and the optical bandwidth 115 nm. The instantaneous linewidth was measured to be 0.2 nm, corresponding to an axial ranging depth of 3.7 mm. A fiber Bragg grating (FBG) was used for trigger signal generation. Fifty percent of the power was directed to the sample arm of the system interferometer and the other half directed to the reference arm. The sample arm consisted of two quarter wave plates (Thorlabs, AQWP05M-1600) as described above, a galvanometer scanner and a 30 mm focusing lens, providing a $1/e^2$ radius of ~ 22 μm. The reference arm utilized a plate beam splitter to provide the reference optical path for the calibration signals E_1' and E_2'. An acousto-optic frequency modulator (AOM, Brimrose Inc. AMF-25-1300) running at 25 MHz was used in the reference arm to remove depth-degeneracy and provide full-range imaging [18]. A polarization-diverse, balanced detection scheme (PDD) was implemented for polarization-sensitive imaging and minimizing polarization dependent fading. A polarizer, orientated at 45° with respect to the polarization eigenstates of the receiver, was located at the reference input port of the detection setup to ensure equal reference arm power for each channel and alleviates reduction of polarization mode dispersion artifacts from the reference signal. Multi-mode fiber was used to provide maximum transmission of the power spectral density after interference. The signal from each 100 MHz balanced receiver (Thorlabs, PDB110C) was acquired by a two-channel digitizer (Signatec PX14400, 14 bits) at a rate of 100 MS/s. The axial resolution was measured to be 10.1 μm in air and the sensitivity was 102 dB. System dispersion was compensated numerically. To accommodate linear birefringence from the galvo mirror reflection, fine-tuning the optical axis of QWP2 adjusted the effective retardation to maintain circular polarization at the sample. PSP-referencing as well as calculation of the output fiber Jones matrix, Jf , was achieved by adjusting the polarization controller in the sample arm and observing the Stokes vectors of $E_{1,2,3}'$ with their corresponding angle in the Poincaré sphere in real-time, using a customized Labview interface. Both Stokes angles were measured over a period of 1 hour and remained consistent within a standard deviation of 3°. Any deviation of $E_{1,2}$ from a horizontal or vertical polarization state was again corrected by PSP-referencing (i.e., $arg \quad min\left\{\leq E_1{}'\mathrm{E}_2{}'\right\} \rightarrow 0^o$ in Stokes space), leading to an updated J_f within a few seconds. Using a manoeuvrable plate beam splitter, the calibration signal structure was located outside the region of interest used for sample imaging.

Figure 4a shows the measured optical axis orientation and retardation of a wave plate specified for quarter wave retardance at 532 nm. Using a custom polarimeter, the retardation of the wave plate was measured to be 39° at 1300 nm. We rotated the wave plate by 180° in 20° steps. The measured retardation stayed constant at 40.5°±0.84° for all set axis orientations with a small reproducible systematic variation. We attribute this variation to imperfect polarization optics. The measured fast- axis orientations also agreed well with the set values. A constant reproducible offset of −30° was noted. Similar offsets have also been identified in previous polarization- sensitive setups [7]. Using a variable wave plate (Bereck compensator 5440, Newport), we measured the retardation for several set retardation values and optical axes orientations. The results are shown in Fig. 4b and agree well with the set values. The set retardation is encoded in different colors and the optical axis given by the polar angle.

Finally, we applied the system to measurements *in vivo* (Fig. 5) of the human finger (a), human proximal nail fold (b), human tooth (c), and swine esophagus *ex vivo* (d). Figure 5 shows intensity images, accumulated retardation plots, †, local retardation, $\partial\delta/\partial_z$, optical axis orientation, θ, and degree of polarization uniformity, DOPU. We can easily identify the birefringent effects within the dermis, as well as the birefringent lower half of the nail plate. Birefringence and fast axis appear disorganized in the dermis. DOPU drops sharply in the stratum corneum but recovers in the dermis. The intensity image of the human tooth nicely illustrates the enamel and underlying dentin. Birefringence appears homogenous but is lower in the enamel compared to the dentin; this is more intuitively demonstrated through the local retardation plot. Similar relations are observed for the optical axis, which remains homogenously distributed across the enamel and appears homogenous but rotated in the dentin. The DOPU remains high in the enamel but is reduced in the dentin. Images of the esophagus clearly show the mucosal epithelium, muscularis mucosa, and submucosa with a homogenous and low birefringence, yet the birefringence in the muscularis propria appears higher. This is also better illustrated in the local retardation plot. Interestingly, the optical axis appears homogenous but rotated between epithelium, mucosa, submucosa and muscularis propria, while the DOPU remains high in the epithelium and sharply drops in the lower layers.

It is worth noticing that the single input state implementation described here can be less sensitive to the birefringence of a layered sample; e.g., if a superficial layer converts the transmitted polarization state to coincide with the optical axis of a subsequent layer. Applications that only require a quasi-stationary sample arm with only marginal changes in the fiber optical path give room for a simplified implementation of fiber-based PS-OCT that does not require multiple input polarization states, active components or PM fiber. In this report we have shown that with the calibration of only a single fiber transformation, the performance of a single-mode fiber-based PS system can equal that of traditional free-space configurations. By referencing the polarization state of the sample arm fiber with the eigenpolarizations of a wave plate, we accommodated the birefringence of the fiber from the source to the sample and solved for the fiber Jones matrix from the sample to the detector. The calibration took only a few seconds and was applied for imaging *in vivo*.

Acknowledgments

This work was supported in part by the National Institute of Health, grant P41 EB015903, and by the Terumo Corporation.

References

1. Hee MR, Huang D, Swanson EA, Fujimoto JG. J. Opt. Soc. Am. B. 1992; 9(6):903–908.
2. de Boer JF, Milner TE, van Gemert MJC, Nelson JS. Opt. Lett. 1997; 22:934–936. [PubMed: 18185711]
3. Cense B, Chen TC, Park BH, Pierce MC, de Boer JF. Opt. Lett. 2002; 27(18):1610–1612. [PubMed: 18026517]
4. Goetzinger E, Pircher M, Geitzenauer W, Ahlers C, Baumann B, Michels S, Schmidt-Erfurth U, Hitzenberger CK. Opt. Express. 2008; 16(21):16410–16422. [PubMed: 18852747]
5. Kim KH, Pierce MC, Maguluri G, Park BH, Yoon SJ, Lydon M, Sheridan R, de Boer JF. J. Biomed. Opt. 2012; 17(6):066012. [PubMed: 22734768]

6. Drexler W, Stamper D, Jesser C, Li X, Pitris C, Saunders K, Martin S, Lodge MB, Fujimoto JG, Brezinski ME. J. Rheumatol. 2001; 28:1311–1318. [PubMed: 11409125]
7. Hitzenberger CK, Goetzinger E, Sticker M, Pircher M, Fercher AF. Opt. Express. 2001; 9:780–790. [PubMed: 19424315]
8. Goetzinger E, Baumann B, Pircher M, Hitzenberger CK. Opt. Express. 2009; 17(25):22704–22717. [PubMed: 20052196]
9. Davé DP, Akkin T, Milner TE. Opt. Lett. 2003; 28(19):1775–1777. [PubMed: 14514097]
10. Saxer CE, de Boer JF, Park BH, Zhao Y, Chen Z, Nelson JS. Opt. Lett. 2000; 25(18):1355–1357. [PubMed: 18066215]
11. Park BH, Pierce MC, Cense B, de Boer JF. Opt. Lett. 2004; 29(21):2512–2514. [PubMed: 15584278]
12. Jiao S, Todorovic M, Stoica G, Wang LV. Appl. Opt. 2005; 44(26):5463–5467. [PubMed: 16161660]
13. Jiao S, G. Stoica W. Yu, Wang LV. Opt. Lett. 2003; 28(14):1206–1208. [PubMed: 12885022]
14. Oh WY, Yun SH, Vakoc BJ, Shishkov M, Desjardins AE, Park BH, de Boer JF, Tearney GJ, Bouma BE. Opt. Express. 2008; 16(2):1096–1103. [PubMed: 18542183]
15. Trasischker W, Zotter S, Torzicky T, Baumann B, Haindl R, Pircher M, Hitzenberger CK. Biomed. Opt. Express. 2014; 5(8):2798–2809. [PubMed: 25136503]
16. Pahlevaninezhad H, Lee AMD, Cahill L, Lam S, MacAulay C, Lane P. Photonics. 2014; 1(4):283–295.
17. Lippok N, Coen S, Leonhardt R, Nielsen P, Vanholsbeeck F. Opt. Lett. 2012; 37(15):3102–3104. [PubMed: 22859099]
18. Yun SH, Tearney GJ, de Boer JF, Bouma BE. Opt. Express. 2004; 12(20):4822–4828. [PubMed: 19484034]

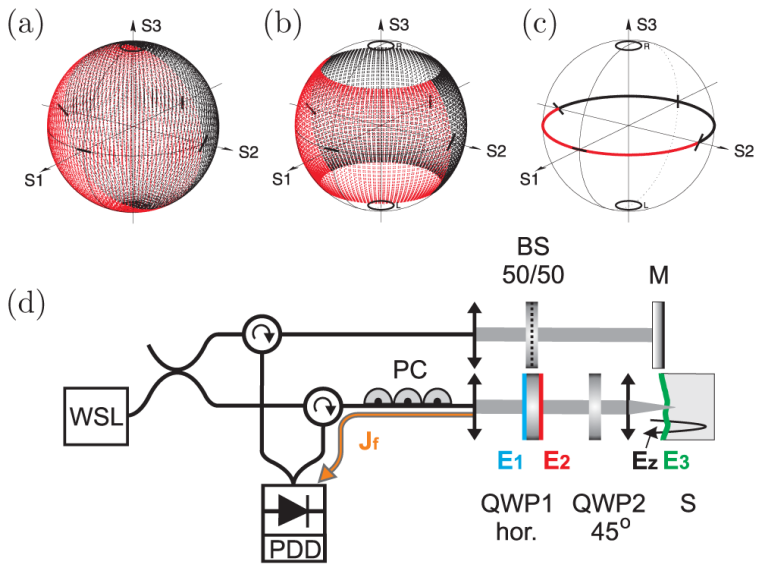

Fig. 1.

(a) PSP (eigenvectors) of a quarter–half–quarter system. (c) PSP of a quarter wave plate. (d) Concept of single input state, single–mode fiber–based PS–OFDI using PSP–referencing: WSL, wavelength swept laser; PC, polarization controller; BS, beam splitter; M, mirror; QWP, quarter wave plate; S, sample; PDD, polarization diverse detection. $E_{1,2,3}$ illustrate three interfaces used for post–processing.

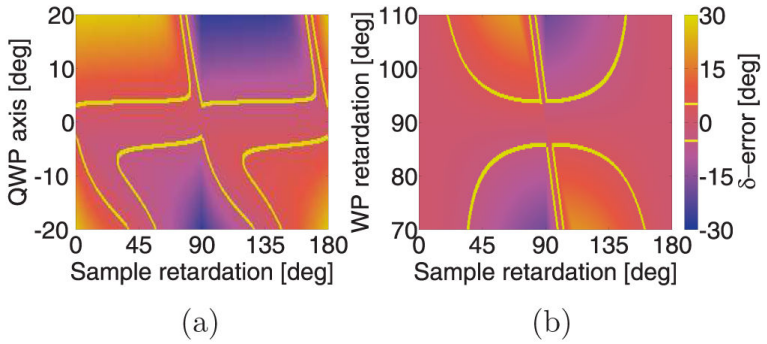

Fig. 2.

Simulated error in calculated sample retardation for different set sample retardation and fast optical axis orientation of QWP1 (a), and different retardation of second wave plate (b). Sample optical axis was 45°. The same colorbar applies to both figures. Yellow lines indicate an error range of ±4°.

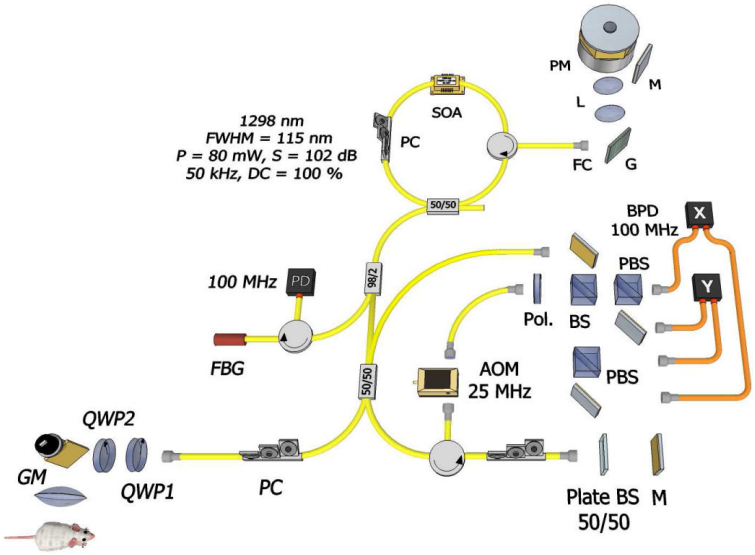

Fig. 3.

Single input state, single–mode fiber PS–OFDI configuration: PM, polygon mirror; M, mirror; L, lens; G, grating; FC, fiber coupler; SOA, semiconductor optical amplifier; PC, polarization controller; FBG, fiber bragg grating; QWP, quarter wave plate; GM, galvo mirror; Plate BS, 50/50 plate beam splitter; AOM, acoustooptic modulator; BS, 50/50 beam splitter; PBS, polarizing beam splitter; PD, photo diode; BPD, balanced photo diode. Single–mode fiber is yellow and multi–mode fiber is orange color coded.

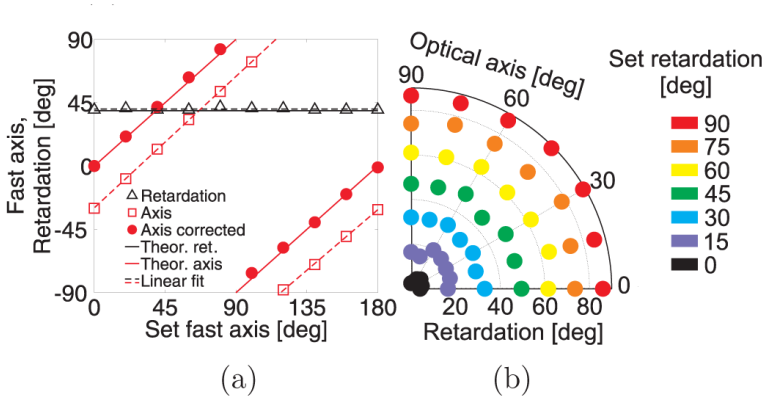

Fig. 4.

(a) Measured retardation and optical axis orientation as a function of set optical axis orientation for a quarter wave plate designed for 532 nm. (b) Measured retardation for various set retardation and optical axis orientations using a variable wave plate.

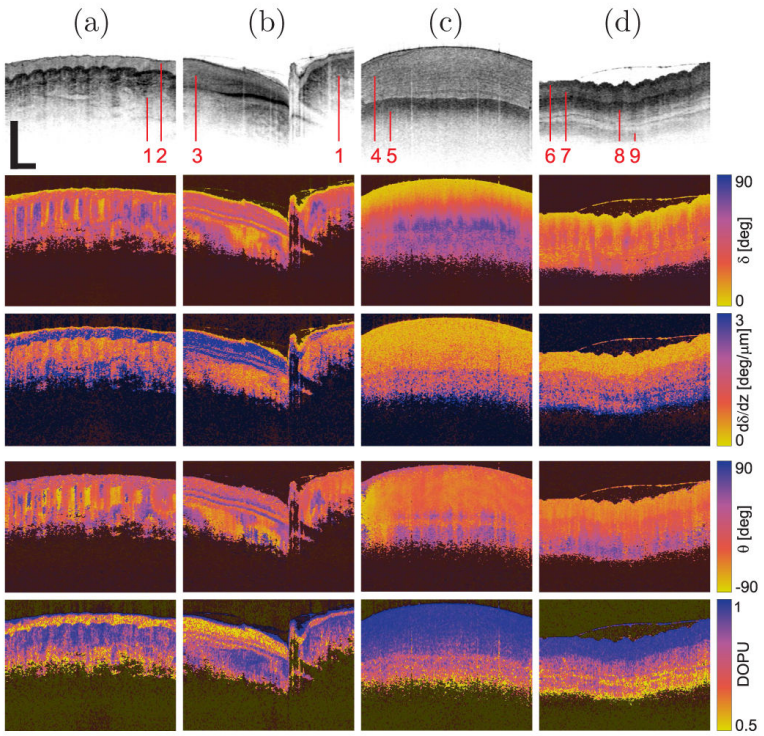

Fig. 5.

OFDI images of biological samples showing plots for intensity, accumulated retardation, †, local retardation, $\partial\delta/\partial_z$, fast axis orientation, θ, and degree of polarization uniformity, DOPU, for human finger (a), human finger nail (b), human tooth (c), swine esophagus (d). 1: dermis; 2: epidermis; 3: nail plate; 4: enamel; 5: dentin; 6: epithelium; 7: muscularis mucosa; 8: submucosa; 9: muscularis propria. Scale bars = 1 mm.